

Speedrunning ImageNet Diffusion

Swayam Bhanded

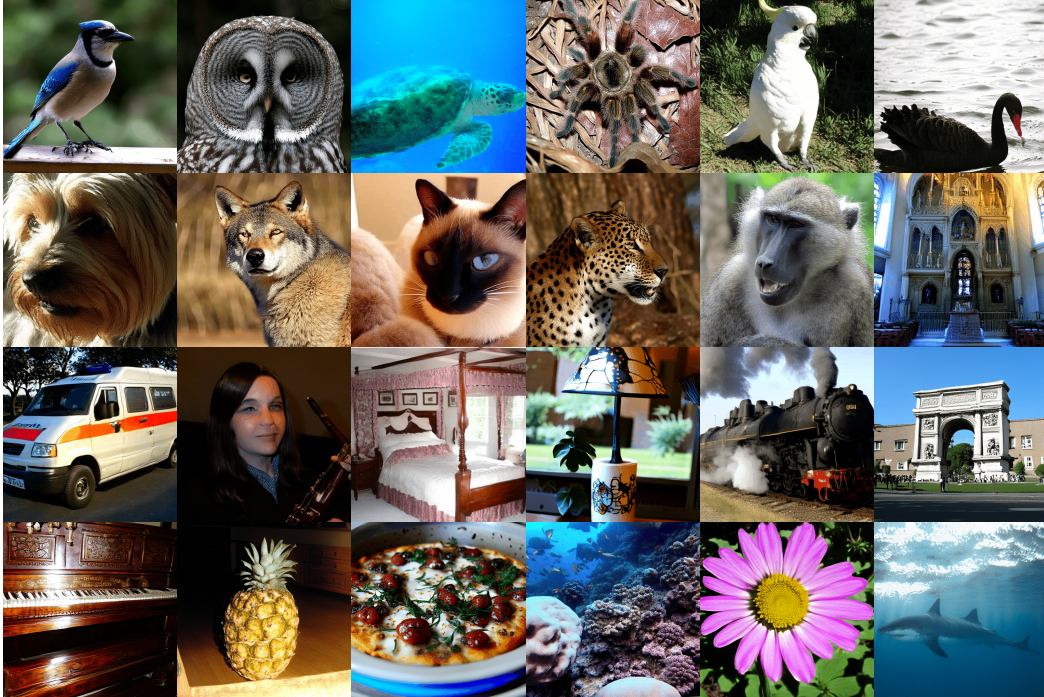


Figure 1: SR-DiT-B/1 samples on ImageNet-512.

Abstract

Recent advances have significantly improved the training efficiency of diffusion transformers. However, these techniques have largely been studied in isolation, leaving unexplored the potential synergies from combining multiple approaches. We present **SR-DiT** (Speedrun Diffusion Transformer), a framework that systematically integrates token routing, architectural improvements, and training modifications on top of representation alignment. Our approach achieves FID 3.49 and KDD 0.319 on ImageNet-256 using only a 140M parameter model at 400K iterations without classifier-free guidance—comparable to results from 685M parameter models trained significantly longer. To our knowledge, this is a state-of-the-art result at this model size. Through extensive ablation studies, we identify which technique combinations are most effective and document both synergies and incompatibilities. We release our framework as a computationally accessible baseline for future research.

Relevant links (code, checkpoints, and experiment logs) are provided in the Resources section.

1 Introduction

Diffusion models have emerged as the dominant paradigm for high-quality image generation, yet their training remains computationally expensive. Recent years have witnessed a proliferation of techniques aimed at accelerating diffusion model training: improved architectures [38], representation alignment [34, 36], better tokenizers [12], and various training modifications. However, these advances have largely been developed and evaluated in isolation, each claiming improvements over increasingly outdated baselines. This fragmented landscape leaves a critical question unanswered: *how do these techniques interact when combined, and what performance is achievable by systematically integrating them?*

The current state of research presents several challenges. First, most techniques are evaluated against vanilla diffusion transformers, ignoring the substantial gains from other concurrent work. Second, flagship results typically require large models (e.g., SiT-XL with 685M parameters) trained for millions of iterations, creating high barriers for academic researchers with limited compute. Third, the interactions between techniques—whether synergistic or redundant—remain poorly understood.

We address these challenges with **SR-DiT** (Speedrun Diffusion Transformer), a framework that systematically combines recent advances to maximize training efficiency. Our key insight is that many techniques target orthogonal aspects of the training process: representation alignment provides strong learning signals, token routing reduces computational redundancy and improves information flow, modern architectures improve optimization dynamics, and semantic tokenizers provide more learnable latent spaces. By carefully integrating these components, we achieve results that rival or exceed large-scale models while using only a fraction of the compute.

Concretely, starting from the SiT-B/1 architecture (130M parameters), we add improvements to finally achieve FID 3.49 on ImageNet-256 at 400K iterations without classifier-free guidance. For comparison, REG [34]—which itself claims $63\times$ convergence speedup over vanilla SiT—requires SiT-XL (685M parameters) to reach FID 3.4, while REPA [36] needs 4 million training steps with SiT-XL to achieve FID 5.9. Our approach thus demonstrates that combining existing techniques intelligently can yield outsized gains, providing a strong and efficient baseline for future research.

Our contributions are:

- A systematic study of how recent diffusion training techniques interact when combined, identifying synergies and incompatibilities.
- An efficient framework achieving FID 3.49 and KDD 0.319 on ImageNet-256 with only 140M parameters at 400K iterations, comparable to much larger models trained for longer.
- Extensive ablations documenting both successful combinations and negative results, providing practical guidance for researchers.
- A computationally accessible baseline enabling faster iteration for academic research.

2 Related Work

Diffusion models. Denoising diffusion probabilistic models [7, 25] and score-based generative models [26, 27] have become the foundation for state-of-the-art image generation. Flow matching [14, 15] provides an alternative formulation with simpler training objectives. The Diffusion Transformer (DiT) [20] demonstrated that transformer architectures can match or exceed U-Net performance, while SiT [16] extended this to flow matching. We build upon SiT as our base architecture.

Representation alignment. REPA [36] introduced the idea of aligning diffusion model hidden states with pretrained vision encoder features, achieving significant training speedups. REG [34] extended this with generative objectives, claiming $63\times$ convergence speedup over vanilla SiT. These methods provide strong learning signals that guide the model toward semantically meaningful representations. We use REG as our starting point and evaluate additional techniques on top.

Semantic latent spaces. The choice of image tokenizer significantly impacts diffusion training dynamics. Standard SD-VAE [21] encodes images into latent spaces optimized for reconstruction, but not necessarily for generation. LightningDiT [35] introduced a VAE trained with semantic objectives, producing latent spaces that are more “diffusible”—easier for diffusion models to learn.

INVAE [12] (from REPA-E) follows this direction with improved semantic properties. These tokenizers accelerate learning by providing latent representations with stronger semantic structure.

Token routing. TREAD [10] demonstrated that routing 50% of tokens to skip intermediate transformer layers both reduces computation and improves convergence—a counterintuitive finding suggesting that full token processing may be redundant. SPRINT [38] introduces architectural modifications that allow increasing the token drop rate to 75%, achieving greater efficiency gains. These methods reveal that diffusion transformers have significant computational slack that can be exploited for efficiency.

Architectural improvements. Modern transformer components from language modeling have shown benefits in vision. LightningDiT incorporates SwiGLU activations [23], RMSNorm [37], and RoPE [30]. QK normalization [5] stabilizes attention, and Value Residual Learning [40] improves information flow. We evaluate how these architectural choices interact with representation alignment and token routing.

3 Background

3.1 Evaluation Metrics

While Fréchet Inception Distance (FID) [6] has been the standard metric for evaluating generative models, recent work has exposed significant limitations in commonly used metrics [28]. Stein et al. demonstrate that among existing metrics, **Kernel DINO Distance (KDD)** correlates most strongly with human perceptual judgments. KDD computes distances between generated and real image distributions using DINOv2 [19] features in a kernel-based framework. Lower KDD values indicate better generation quality. We report both KDD and traditional metrics (FID, sFID, IS, Precision, Recall) for comprehensive evaluation.

3.2 Diffusion / Flow Matching

We follow SiT [16] and train the model with a flow-matching objective using velocity prediction. Given a clean input x (VAE latents) and a timestep $t \in [0, 1]$, we construct a noisy sample using an interpolant

$$x_t = \alpha(t) x + \sigma(t) \epsilon, \quad \epsilon \sim \mathcal{N}(0, I), \quad (1)$$

where $\alpha(t), \sigma(t)$ define the path (e.g., linear or cosine). The corresponding velocity target is

$$v_t^* = \dot{\alpha}(t) x + \dot{\sigma}(t) \epsilon. \quad (2)$$

The base training loss is mean-squared error on velocity prediction, $\mathbb{E}[\|v_\theta(x_t, t) - v_t^*\|_2^2]$.

3.3 Time Shifting

We use time shifting [3] to reweight which timesteps the model sees, reducing over-emphasis on high-SNR (easy) denoising steps. We first sample $t \sim \mathcal{U}(0, 1)$, then apply the monotone transform

$$t' = \frac{s t}{1 + (s - 1)t}, \quad s = \sqrt{\frac{D}{4096}}, \quad D = C \cdot H \cdot W, \quad (3)$$

which (for $s > 1$) shifts mass toward larger t (noisier / lower-SNR inputs). We apply the same transformation during both training and sampling. Following Zheng et al. [39], we compute the shift factor from the full latent dimensionality (including channels) and use 4096 as the reference dimension.

3.4 Rotary Position Embeddings (RoPE)

Rotary position embeddings (RoPE) [30] encode positional information by rotating query and key vectors in multi-head attention. For a token at position i and head vector q_i (and similarly k_i), RoPE rotates each consecutive 2D pair via

$$\text{RoPE}(q_i) = q_i \odot \cos \omega_i + \text{rot}(q_i) \odot \sin \omega_i, \quad \text{rot}([x_{2j}, x_{2j+1}]) = [-x_{2j+1}, x_{2j}], \quad (4)$$

where ω_i are position-dependent frequencies and \odot is elementwise multiplication. For images, we use a 2D extension where positions i correspond to indices on the flattened $H \times W$ patch grid.

3.5 RMSNorm

RMSNorm [37] is a normalization layer that scales activations by their root-mean-square (without mean-centering), which reduces computation and can improve stability. For an input vector $x \in \mathbb{R}^d$, RMSNorm computes

$$\text{RMSNorm}(x) = g \odot \frac{x}{\sqrt{\frac{1}{d} \sum_{j=1}^d x_j^2 + \epsilon}}, \quad (5)$$

where g is a learned gain parameter and ϵ is a small constant.

3.6 Value Residual Learning

Value Residual Learning [40] modifies attention by injecting a residual connection across the *value* stream. The method caches the value vectors from an early attention block and reuses them as a reference value for subsequent blocks. Let $v^{(\ell)}$ denote the value vectors produced by block ℓ (after the value projection) and let $v^{(0)}$ denote the cached reference values (from the first block). We form a mixed value

$$\tilde{v}^{(\ell)} = \lambda v^{(0)} + (1 - \lambda) v^{(\ell)}, \quad (6)$$

with a learned scalar $\lambda \in [0, 1]$ (implemented as a learnable parameter). Attention then uses $\tilde{v}^{(\ell)}$ in place of $v^{(\ell)}$.

3.7 Token Routing and Path-Drop Guidance

TREAD [10] and SPRINT [38] implement token routing by temporarily dropping a large fraction of tokens in the middle transformer blocks: a dense prefix processes all tokens, then only the retained (sparse) tokens are propagated through a sequence of mid blocks, and the dropped tokens are reintroduced for the final blocks. SPRINT improves this reintroduction step by padding the sparse sequence back to the full length with a learned [MASK] token and explicitly fusing the padded sparse stream with the dense stream (e.g., concatenation followed by a projection).

We also use *path-drop guidance* (PDG), a CFG-style heuristic in which the unconditional prediction is intentionally weakened by skipping the routed mid blocks entirely (i.e., dropping the sparse path). Let $v_\theta(x_t, t, c)$ denote the conditional model prediction under class conditioning c (sparse path enabled) and $v_\theta^{\text{weak}}(x_t, t)$ the unconditional prediction computed with the routed mid blocks skipped. The guided prediction is

$$v_\theta^{\text{guide}}(x_t, t, c) = v_\theta^{\text{weak}}(x_t, t) + s (v_\theta(x_t, t, c) - v_\theta^{\text{weak}}(x_t, t)), \quad (7)$$

where s is the guidance scale. Importantly, we use PDG **only for qualitative sampling** (visualizations) and **do not** use PDG for the quantitative metrics reported in the paper.

3.8 Contrastive Flow Matching

Contrastive Flow Matching (CFM) [29] introduces an additional training objective that improves convergence speed. The CFM loss is computed by contrasting model outputs with random targets:

$$\mathcal{L}_{\text{CFM}} = -\lambda \mathbb{E} \left[\|v_\theta(x_t, t) - \hat{v}_{\text{target}}\|^2 \right] \quad (8)$$

where \hat{v}_{target} is a random training target unrelated to x_t (obtained by shuffling the minibatch of the velocity target elementwise), and λ is a weighting coefficient (default 0.05). The negative sign encourages the model to maximize distance from other samples' predictions.

3.9 Representation Alignment (REPA and REG)

We build on Representation Alignment for Generation (REPA) [36] and its extension REG [34], which add an auxiliary representation objective to the standard denoising / flow-matching loss. We use the same noising process and velocity-prediction objective described above.

For the representation targets, we pass the *clean* image through a frozen vision encoder (DINOv2 [19]) to obtain per-token targets z (and a global CLS embedding c_{cls}). The diffusion transformer produces intermediate hidden states that are mapped through small MLP projectors to predicted representations \tilde{z} . REPA uses a projection loss based on cosine similarity:

$$\mathcal{L}_{\text{REPA}} = -\lambda_{\text{REPA}} \frac{1}{M} \sum_{m=1}^M \left\langle \frac{z_m}{\|z_m\|_2}, \frac{\tilde{z}_m}{\|\tilde{z}_m\|_2} \right\rangle, \quad (9)$$

where m indexes tokens and we use $\lambda_{\text{REPA}} = 0.5$ by default.

REG extends this setup by also diffusing the DINO CLS embedding alongside the latents.

4 Method

Our approach systematically combines recent advances to maximize training efficiency. We start from REG [34] with INVAE [12] as our baseline, then progressively add architectural improvements and training objective modifications.

4.1 Architectural Improvements

We evaluate several modern transformer components that have shown benefits in language and vision models:

SPRINT [38]: We use SPRINT token routing with a drop ratio of 0.75 (keeping 25% tokens) in the sparse path. Following the standard SPRINT split, we run 2 dense “encoder” blocks on all tokens, route over the middle blocks (operating on the sparse subset, then padding back and fusing), and run 2 dense “decoder” blocks on the fused full sequence.

RMSNorm [37]: Starting from our fork of the REG baseline, we replace all LayerNorm instances in the backbone with RMSNorm. Concretely, this includes: (i) the two per-block normalizations before attention and before the MLP in every transformer block (norm1, norm2); (ii) the per-head query/key normalizers used by QK Norm (q_norm, k_norm); (iii) the final normalization before the output projection (norm_final); and (iv) the RMSNorm applied to the REG-diffused CLS embedding before concatenation (wg_norm).

Rotary Position Embeddings (RoPE) [30]: We use 2D RoPE (see Section 3.4) via the EVA-02-style implementation [4], later adapted by the TREAD authors to support routed / sparse token subsets for their LightningDiT+TREAD experiments [10, 35].⁰ In routed blocks, we pass per-token indices `rope_ids` so each retained token is rotated using its original spatial position. We further modify the implementation to exclude the leading class token (the REG-diffused CLS embedding) from rotation.

QK Normalization [5]: Normalizing query and key vectors before computing attention scores stabilizes training dynamics.

Value Residual Learning [40]: Adding a residual connection around the value projection improves gradient flow and model expressiveness.

These components were proposed independently in various contexts; our contribution is evaluating their interactions when combined with representation alignment and token routing.

4.2 Training Objective

We incorporate Contrastive Flow Matching (CFM) [29], which adds an auxiliary loss that improves convergence speed (see Section 3). Overall, our training loss is

$$\mathcal{L} = \mathcal{L}_{\text{vel}} + \lambda_{\text{REPA}} \mathcal{L}_{\text{REPA}} + \lambda_{\text{cls}} \mathcal{L}_{\text{cls}} + \lambda_{\text{CFM}} \mathcal{L}_{\text{CFM}}, \quad (10)$$

where \mathcal{L}_{vel} is the standard velocity-prediction MSE on latents (Section 3), $\mathcal{L}_{\text{REPA}}$ is the projection loss (Section 3), \mathcal{L}_{cls} is the velocity-prediction MSE for the REG-diffused CLS embedding, and \mathcal{L}_{CFM} is the contrastive term. We use $\lambda_{\text{REPA}} = 0.5$, $\lambda_{\text{cls}} = 0.03$, and $\lambda_{\text{CFM}} = 0.05$.

⁰https://github.com/flixmkl/lightningDiT_TREAD/blob/main/models/pos_embed_tread.py

Table 1: Performance comparison on ImageNet-256 at 400K iterations. Lower FID/sFID/KDD and higher IS/Precision/Recall are better. All methods evaluated at NFE=250 without CFG or PDG.

Method	#Params	FID \downarrow	sFID \downarrow	IS \uparrow	Prec. \uparrow	Rec. \uparrow	KDD \downarrow
<i>Baselines (SiT-B/2, SD-VAE)</i>							
SiT-B/2	130M	33.0	6.46	43.7	0.53	0.63	–
+ REPA	130M	24.4	6.40	59.9	0.59	0.65	–
+ REG	132M	15.2	6.69	94.6	0.64	0.63	–
<i>SR-DiT (SiT-B/I, INVAE)</i>							
REG + INVAE	132M	10.56	<u>5.49</u>	104.5	0.691	0.632	0.586
+ SPRINT	140M	4.58	<u>7.04</u>	188.7	0.760	0.562	0.385
+ RMSNorm	140M	4.56	<u>6.58</u>	186.8	0.772	0.562	0.381
+ RoPE	140M	4.09	6.22	194.2	0.778	<u>0.563</u>	0.368
+ QK Norm	140M	4.02	6.18	193.5	0.784	<u>0.563</u>	0.364
+ Value Residual	140M	3.64	5.98	202.0	0.798	<u>0.560</u>	0.353
+ CFM	140M	3.61	5.26	<u>211.9</u>	0.817	0.536	0.319
+ Time Shifting	140M	<u>3.56</u>	5.64	209.6	0.807	0.550	0.336
+ Balanced Sampling	140M	3.49	5.67	221.2	<u>0.808</u>	0.546	<u>0.332</u>

4.3 Time Shifting

We apply time shifting (Section 3.3) during both training and sampling.

5 Experiments

5.1 Experimental Setup

We conduct experiments on ImageNet-256 [2]. We build upon the SiT-B [16] and REG [34] architecture and compare our ablations against multiple baselines. Our model uses the SiT-B/1 architecture (patch size 1 instead of 2), starting with 132M parameters for the baseline, as INVAE has $16\times$ spatial compression compared to SD-VAE [21]’s $8\times$ compression. SPRINT modifications increase the model to 140M parameters. This architecture choice significantly reduces computational costs compared to larger models like SiT-XL (685M parameters) while maintaining strong performance.

Training the final SR-DiT-B/1 architecture to 400K iterations took approximately 10 hours on a single node with $8\times$ NVIDIA H200 GPUs for ImageNet-256 (80 GPU-hours), and approximately 15 hours for ImageNet-512 (120 GPU-hours).

We evaluate generation quality using Kernel DINO Distance (KDD) as our primary metric, along with standard metrics: Fréchet Inception Distance (FID) [6], spatial FID (sFID) [18], Inception Score (IS) [22], Precision, and Recall [11]. All metrics are computed on 50K generated samples. Following RAE [39], we use balanced label sampling during generation for metric calculation, ensuring each class is equally represented in the generated samples. This corrects an implementation detail where random sampling can lead to imbalanced class distributions, improving FID marginally. **All results are reported without CFG or PDG.**

5.2 Results

We use REG with INVAE as our base configuration and systematically evaluate architectural and training improvements. Table 1 presents our main results at 400K iterations, comparing against SiT-B/2 baselines.

In addition to ImageNet-256, we evaluate SR-DiT-B/1 on ImageNet-512 using the same training setup scaled to 512×512 resolution. We compare against the DiT-XL/2 and U-DiT-B baselines reported in U-DiT [31] as these are the only reported results we could find for FID-50k on ImageNet-512 at 400k iterations. As shown in Table 2, SR-DiT-B/1 achieves strong ImageNet-512 performance. All results are evaluated without CFG or PDG.

Figure 3 qualitatively illustrates how our final architecture sharpens details and improves semantic fidelity over the REG + INVAE baseline under identical sampling conditions.

Table 2: Performance comparison on ImageNet-512 at 400K iterations. Baseline results for DiT-XL/2* and U-DiT-B are taken from U-DiT-Bs [31]. Lower FID/sFID/KDD and higher IS/Precision/Recall are better.

Method	FID \downarrow	sFID \downarrow	IS \uparrow	Prec. \uparrow	Rec. \uparrow	KDD \downarrow
DiT-XL/2*	20.94	6.78	66.30	0.745	0.581	–
U-DiT-B	15.39	6.86	92.73	0.756	0.605	–
SR-DiT-B/1 (ours)	4.23	5.46	192.34	0.839	0.531	0.306

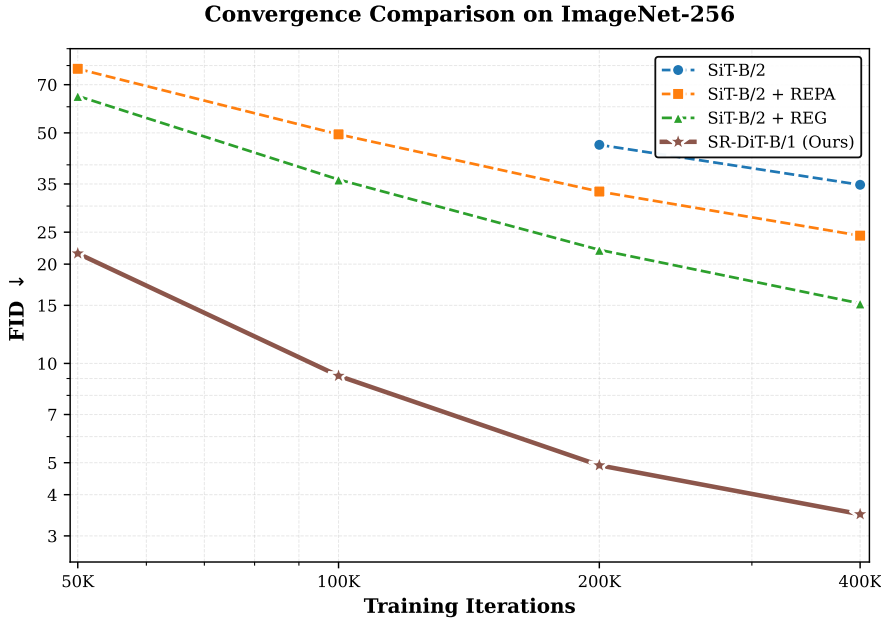


Figure 2: Training convergence comparison on ImageNet-256. SR-DiT-B/1 achieves strong performance with substantial convergence speedup.

Baseline comparison. The original SiT-B/2 [16] with 130M parameters requires 400K iterations to achieve FID 33.0. REPA [36] improves this to FID 24.4, while REG [34] reaches FID 15.2 at 400K iterations with 132M parameters. Our baseline configuration (REG + INVAE) with SiT-B/1 achieves FID 10.56 using 132M parameters, already surpassing REG with SD-VAE at the same parameter count.

5.3 Analysis

What matters most. The dominant improvement comes from representation alignment and entanglement (REPA/REG), token routing (SPRINT), and from using a semantic VAE (INVAE)

Other components help cumulatively. RMSNorm, RoPE, QK Norm, and Value Residual are individually modest but consistently beneficial in our setting, improving optimization stability and information flow when stacked.

6 Discussion

6.1 Limitations and Future Work

While our results demonstrate strong improvements, several avenues remain for future exploration:



Figure 3: Qualitative comparison between our REG + INVAE starting point (top row) and the final SR-DiT-B/1 architecture (bottom row) on ImageNet-256 at 400K training iterations. Generated without CFG or PDG, using the same random seed and class label for both models.

Scaling to larger models. While we focus on the efficient SiT-B/1 architecture, investigating whether these improvements transfer to larger models (SiT-L, SiT-XL) would be valuable for understanding scalability.

Text to image generation. Extending these techniques to text-to-image generation would demonstrate generalization and practical utility.

Further optimizations. There are numerous other techniques which we did not explore due to a lack of time and resources. Future work can investigate these techniques to further improve performance.

7 Conclusion

We present SR-DiT, a framework that achieves efficient diffusion model training by combining representation alignment with modern architectural improvements and training modifications. Starting from REG with INVAE (132M parameters), we demonstrate that progressive modifications (SPRINT, RMSNorm, RoPE, QK Norm, Value Residual, CFM, Time Shifting, Balanced Sampling) create strong synergies, achieving FID 3.49 and KDD 0.319 on ImageNet-256 with the efficient SiT-B/1 architecture (140M parameters). We also adopt KDD as a more reliable evaluation metric. Our systematic ablations identify which components contribute most to performance gains, providing insights for future work in efficient diffusion model training.

Resources

Code, checkpoints, and experiment logs are available at:

- **GitHub (final SR-DiT code):** <https://github.com/SwayStar123/SpeedrunDiT>
- **Checkpoints:** <https://huggingface.co/SwayStar123/SpeedrunDiT/tree/main>
- **Weights & Biases runs:** <https://wandb.ai/kagaku-ai/REG>

Original code for the full set of ablations can be found as branches in <https://github.com/SwayStar123/REG>; the final architecture was consolidated into the SpeedrunDiT repository.

Acknowledgments and Disclosure of Funding

We gratefully acknowledge support from WayfarerLabs (<https://wayfarerlabs.ai>), also known as Open World Labs, for sponsoring the compute resources used in this work.

References

- [1] Hesen Chen, Junyan Wang, Zhiyu Tan, and Hao Li. Sara: Structural and adversarial representation alignment for training-efficient diffusion models. *arXiv preprint arXiv:2503.08253*, 2025.
- [2] Jia Deng, Wei Dong, Richard Socher, Li-Jia Li, Kai Li, and Li Fei-Fei. Imagenet: A large-scale hierarchical image database. In *2009 IEEE Conference on Computer Vision and Pattern Recognition*, pages 248–255, 2009.
- [3] Patrick Esser, Sumith Kulal, Andreas Blattmann, Rahim Entezari, Jonas Müller, Harry Saini, Yam Levi, Dominik Lorenz, Axel Sauer, Frederic Boesel, Dustin Podell, Tim Dockhorn, Zion English, Kyle Lacey, Alex Goodwin, Yannik Marek, and Robin Rombach. Scaling rectified flow transformers for high-resolution image synthesis. *arXiv preprint arXiv:2403.03206*, 2024.
- [4] Yuxin Fang, Quan Sun, Xinggang Wang, Tiejun Huang, Xinlong Wang, and Yue Cao. Eva-02: A visual representation for neon genesis. *arXiv preprint arXiv:2303.11331*, 2023. URL <https://arxiv.org/abs/2303.11331>.
- [5] Alex Henry, Prudhvi Raj Dachapally, Shubham Pawar, and Yuxuan Chen. Query-key normalization for transformers. *arXiv preprint arXiv:2010.04245*, 2020.
- [6] Martin Heusel, Hubert Ramsauer, Thomas Unterthiner, Bernhard Nessler, and Sepp Hochreiter. Gans trained by a two time-scale update rule converge to a local nash equilibrium. In *Advances in Neural Information Processing Systems*, pages 6626–6637, 2017.
- [7] Jonathan Ho, Ajay Jain, and Pieter Abbeel. Denoising diffusion probabilistic models. In *Advances in Neural Information Processing Systems*, 2020.
- [8] Allen Hao Huang and Imanol Schlag. Deriving activation functions using integration. *arXiv preprint arXiv:2411.13010*, 2024.
- [9] Keller Jordan. Muon optimizer. <https://x.com/kellerjordan0/status/1842300916864844014>, 2024.
- [10] Felix Krause, Timy Phan, Ming Gui, Stefan Andreas Baumann, Vincent Tao Hu, and Björn Ommer. Tread: Token routing for efficient architecture-agnostic diffusion training. *arXiv preprint arXiv:2501.04765*, 2025.
- [11] Tuomas Kynkänniemi, Tero Karras, Samuli Laine, Jaakko Lehtinen, and Timo Aila. Improved precision and recall metric for assessing generative models. In *Advances in Neural Information Processing Systems*, pages 3927–3936, 2019.
- [12] Xingjian Leng, Jaskirat Singh, Yunzhong Hou, Zhenchang Xing, Saining Xie, and Liang Zheng. Repa-e: Unlocking vae for end-to-end tuning with latent diffusion transformers. *arXiv preprint arXiv:2504.10483*, 2025.
- [13] Tianhong Li and Kaiming He. Back to basics: Let denoising generative models denoise. *arXiv preprint arXiv:2511.13720*, 2024.
- [14] Yaron Lipman, Ricky T. Q. Chen, Heli Ben-Hamu, Maximilian Nickel, and Matthew Le. Flow matching for generative modeling. In *International Conference on Learning Representations*, 2023.
- [15] Xingchao Liu, Chengyue Gong, and Qiang Liu. Flow straight and fast: Learning to generate and transfer data with rectified flow. *arXiv preprint arXiv:2209.03003*, 2022.
- [16] Nanye Ma, Mark Goldstein, Michael S. Albergo, Nicholas M. Boffi, Eric Vanden-Eijnden, and Saining Xie. Sit: Exploring flow and diffusion-based generative models with scalable interpolant transformers. *arXiv preprint arXiv:2401.08740*, 2024. URL <https://arxiv.org/abs/2401.08740>.
- [17] Konstantin Mishchenko and Aaron Defazio. Prodigy: An expeditiously adaptive parameter-free learner. *arXiv preprint arXiv:2306.06101*, 2023.

[18] Charlie Nash, Jacob Menick, Sander Dieleman, and Peter W Battaglia. Generating images with sparse representations. *arXiv preprint arXiv:2103.03841*, 2021.

[19] Maxime Oquab, Timothée Darcet, Théo Moutakanni, Huy Vo, Marc Szafraniec, Vasil Khalidov, Pierre Fernandez, Daniel Haziza, Francisco Massa, Alaaeldin El-Nouby, et al. Dinov2: Learning robust visual features without supervision. *arXiv preprint arXiv:2304.07193*, 2023.

[20] William Peebles and Saining Xie. Scalable diffusion models with transformers. In *Proceedings of the IEEE/CVF International Conference on Computer Vision*, pages 4195–4205, 2023.

[21] Robin Rombach, Andreas Blattmann, Dominik Lorenz, Patrick Esser, and Björn Ommer. High-resolution image synthesis with latent diffusion models. In *Proceedings of the IEEE Conference on Computer Vision and Pattern Recognition*, pages 10684–10695, 2022.

[22] Tim Salimans, Ian Goodfellow, Wojciech Zaremba, Vicki Cheung, Alec Radford, and Xi Chen. Improved techniques for training gans. In *Advances in Neural Information Processing Systems*, pages 2234–2242, 2016.

[23] Noam Shazeer. Glu variants improve transformer. *arXiv preprint arXiv:2002.05202*, 2020.

[24] David R. So, Wojciech Manke, Hanxiao Liu, Zihang Dai, Noam Shazeer, and Quoc V. Le. Primer: Searching for efficient transformers for language modeling. *arXiv preprint arXiv:2109.08668*, 2021.

[25] Jascha Sohl-Dickstein, Eric A. Weiss, Niru Maheswaranathan, and Surya Ganguli. Deep unsupervised learning using nonequilibrium thermodynamics. In *Proceedings of the 32nd International Conference on Machine Learning*, pages 2256–2265, 2015.

[26] Yang Song and Stefano Ermon. Generative modeling by estimating gradients of the data distribution. In *Advances in Neural Information Processing Systems*, pages 11895–11907, 2019.

[27] Yang Song, Jascha Sohl-Dickstein, Diederik P. Kingma, Abhishek Kumar, Stefano Ermon, and Ben Poole. Score-based generative modeling through stochastic differential equations. In *International Conference on Learning Representations*, 2021.

[28] George Stein, Jesse C Cresswell, Rasa Hosseinzadeh, Yi Sui, Brendan Leigh Ross, Valentin Villegas, Zhaoyan Liu, Anthony L Caterini, J Eric T Taylor, and Gabriel Loaiza-Ganem. Exposing flaws of generative model evaluation metrics and their unfair treatment of diffusion models. *arXiv preprint arXiv:2306.04675*, 2023.

[29] George Stoica, Vivek Ramanujan, Xiang Fan, Ali Farhadi, Ranjay Krishna, and Judy Hoffman. Contrastive flow matching. *arXiv preprint arXiv:2506.05350*, 2025.

[30] Jianlin Su, Yu Lu, Shengfeng Pan, Ahmed Murtadha, Bo Wen, and Yunfeng Liu. Roformer: Enhanced transformer with rotary position embedding. *arXiv preprint arXiv:2104.09864*, 2021.

[31] Yuchuan Tian, Zhijun Tu, Hanting Chen, Jie Hu, Chao Xu, and Yunhe Wang. U-dits: Downsample tokens in u-shaped diffusion transformers, 2024. URL <https://arxiv.org/abs/2405.02730>.

[32] Runqian Wang and Yilun Du. Equilibrium matching: Generative modeling with implicit energy-based models. *arXiv preprint arXiv:2510.02300*, 2024.

[33] Runqian Wang and Kaiming He. Diffuse and disperse: Image generation with representation regularization. *arXiv preprint arXiv:2506.09027*, 2025.

[34] Ge Wu, Shen Zhang, Ruijing Shi, Shanghua Gao, Zhenyuan Chen, Lei Wang, Zhaowei Chen, Hongcheng Gao, Yao Tang, Jian Yang, Ming-Ming Cheng, and Xiang Li. Representation entanglement for generation: Training diffusion transformers is much easier than you think. *arXiv preprint arXiv:2507.01467*, 2025.

[35] Jingfeng Yao, Bin Yang, and Xinggang Wang. Reconstruction vs. generation: Taming optimization dilemma in latent diffusion models. *arXiv preprint arXiv:2501.01423*, 2025.

[36] Sihyun Yu, Sangkyung Kwak, Huiwon Jang, Jongheon Jeong, Jonathan Huang, Jinwoo Shin, and Saining Xie. Representation alignment for generation: Training diffusion transformers is easier than you think. *arXiv preprint arXiv:2410.06940*, 2024.

[37] Biao Zhang and Rico Sennrich. Root mean square layer normalization. *arXiv preprint arXiv:1910.07467*, 2019.

[38] Yandong Zhang, Jing Wang, Junjie Zhang, Xiang Li, and Zhaowei Chen. Sprint: Sparse-dense residual fusion for efficient diffusion transformers. *arXiv preprint arXiv:2510.21986*, 2024.

[39] Boyang Zheng, Nanye Ma, Shengbang Tong, and Saining Xie. Diffusion transformers with representation autoencoders. *arXiv preprint arXiv:2510.11690*, 2024.

[40] Zhanchao Zhou, Tianyi Wu, Zhiyun Jiang, Fares Obeid, and Zhenzhong Lan. Value residual learning. *arXiv preprint arXiv:2410.17897*, 2024.

A Additional Results

This appendix documents additional quantitative results that complement the main text.

A.1 Intermediate SR-DiT-B/1 Training Checkpoints

Table 3 reports SR-DiT-B/1 performance at intermediate training checkpoints, along with the baseline diffusion transformers and the final SR-DiT-B/1 model at 400K iterations.

Table 3: SR-DiT performance at intermediate training checkpoints on ImageNet-256. Lower FID/sFID/KDD and higher IS/Precision/Recall are better. All methods evaluated at NFE=250 without CFG or PDG.

Method	Iter.	FID \downarrow	sFID \downarrow	IS \uparrow	Prec. \uparrow	Rec. \uparrow	KDD \downarrow
SiT-B/2	400K	33.0	6.46	43.7	0.530	0.630	–
+ REPA	400K	24.4	6.40	59.9	0.590	0.650	–
+ REG	400K	15.2	6.69	94.6	0.640	0.630	–
SR-DiT-B/1	50K	21.55	7.75	61.37	0.677	0.475	0.926
SR-DiT-B/1	100K	9.17	6.52	124.69	0.767	0.484	0.584
SR-DiT-B/1	200K	4.91	5.95	184.05	0.801	0.523	0.408
SR-DiT-B/1 (final)	400K	3.49	5.49	221.2	0.808	0.546	0.332

B Additional Ablations

This section documents ablation experiments that did not yield improvements, providing insights into which techniques are less effective when combined with representation alignment.

B.1 Alternative Activations

We evaluated replacing standard feedforward activations with SwiGLU [23], as proposed in LightningDiT. Table 4 shows results at 400K iterations.

Table 4: SwiGLU activation ablation at 400K iterations. Both experiments use REG + INVAE + SPRINT (140M parameters). SwiGLU shows marginal improvement with noticeable training slowdown.

Method	FID \downarrow	sFID \downarrow	IS \uparrow	Prec. \uparrow	Rec. \uparrow	KDD \downarrow
SPRINT (baseline)	4.58	7.04	188.7	0.760	0.562	0.385
+ SwiGLU	4.65	6.84	185.1	0.759	0.568	0.385

SwiGLU showed marginal differences in performance metrics. While sFID improved slightly (6.84 vs 7.04) and KDD remained identical (0.385), FID slightly degraded (4.65 vs 4.58) and IS decreased

(185.1 vs 188.7). Given these mixed results and a noticeable slowdown in training speed, we excluded SwiGLU from our final framework. The minimal performance differences did not justify the computational overhead.

We also tested additional activation variants. Table 5 shows results at 400K iterations.

Table 5: Alternative activation ablations at 400K iterations. All experiments use REG + INVAE + SPRINT + RMSNorm + RoPE + QK Norm. Standard GELU achieves the best compatibility with Value Residual.

Activation	FID \downarrow	sFID \downarrow	IS \uparrow	Prec. \uparrow	Rec. \uparrow	KDD \downarrow
GELU (baseline)	4.02	6.18	193.5	0.784	0.563	0.364
RELU ²	3.81	6.47	198.4	0.778	0.572	0.351
XieLU	4.10	6.35	191.4	0.783	0.562	0.357
Lopsided Leaky RELU ²	4.11	6.67	189.4	0.768	0.569	0.366

RELU² incompatibility with Value Residual. We tested RELU² [24], which initially showed strong results (FID 3.81, KDD 0.351). However, when combined with Value Residual Learning, performance degraded significantly (FID 3.81 \rightarrow 3.81, IS 198.4 \rightarrow 195.1, KDD 0.351 \rightarrow 0.355). In contrast, standard GELU with Value Residual achieved superior results (FID 3.64, IS 202.0, KDD 0.353). Since Value Residual provides larger gains than RELU² alone, we adopted GELU as our activation function. This incompatibility suggests that RELU² and Value Residual may optimize overlapping aspects of the model, leading to diminishing returns when combined.

XieLU. We tested XieLU [8], a recently proposed activation function derived through integration principles. While XieLU achieved competitive results (FID 4.10, KDD 0.357), it underperformed RELU² across most metrics and exhibited noticeably slower training speed. The performance gap and computational overhead made it unsuitable for our framework.

Lopsided Leaky RELU². We tested a variant of RELU² with negative slope handling, defined as:

$$f(x) = \begin{cases} x^2 & \text{if } x > 0 \\ \alpha x & \text{if } x \leq 0 \end{cases} \quad (11)$$

where we use $\alpha = 0.01$. While this variant showed marginally better training loss (approximately 0.0005 lower) than standard RELU², evaluation metrics were noticeably worse across all measures (FID 4.11 vs 3.81, KDD 0.366 vs 0.351). This discrepancy indicates the variant is prone to overfitting. We document this negative result because multiple researchers have independently experimented with this exact variation without success, yet no published work references it. By publishing this result, we hope to prevent others from expending computational resources on this unpromising direction.

B.2 Dispersive Loss

The dispersive loss [33] for improving representation diversity yielded negligible performance differences compared to our baseline, confirming that representation alignment from REG already provides sufficient diversity in the learned representations.

B.3 SARA Structural Loss

We evaluated SARA’s autocorrelation-based structural loss [1], which encourages structural coherence in generated images. Table 6 shows results at 400K iterations with different loss weights. The adversarial component of SARA caused training instability and was excluded.

At the default weight ($\lambda = 0.5$), most metrics degraded slightly despite a marginal KDD improvement. Reducing the weight to $\lambda = 0.25$ further degraded performance across most metrics.

B.4 Alternative Training Objectives

We evaluated alternative training objectives beyond standard flow matching to determine if they could improve generation quality or training efficiency.

Table 6: SARA structural loss ablation at 400K iterations. All experiments use REG + INVAE + SPRINT + RMSNorm + RoPE + QK Norm + Value Residual. The structural loss does not improve upon the baseline.

Method	FID \downarrow	sFID \downarrow	IS \uparrow	Prec. \uparrow	Rec. \uparrow	KDD \downarrow
Baseline	3.64	5.98	202.0	0.798	0.560	0.353
+ SARA ($\lambda = 0.5$)	3.71	6.07	200.1	0.793	0.553	0.351
+ SARA ($\lambda = 0.25$)	3.80	6.00	195.6	0.786	0.563	0.361

Time-Weighted Contrastive Flow Matching (TCFM). We hypothesized that CFM’s contrastive loss might be detrimental at low noise levels, where it could perturb the learned flow even when the clean image structure is already well-defined. We proposed Time-Weighted CFM (TCFM), which reduces the CFM influence as samples approach the clean image:

$$\mathcal{L}_{\text{TCFM}} = -t \cdot \lambda \mathbb{E} \left[\|v_\theta(x_t, t) - \hat{v}_{\text{target}}\|^2 \right] \quad (12)$$

where $t \in [0, 1]$ is the noise timestep. To compensate for the average weighting being halved, we increased λ from 0.05 to 0.10. Table 7 shows results comparing CFM and TCFM.

Table 7: CFM vs TCFM ablation at 400K iterations. TCFM does not improve upon standard CFM.

Method	FID \downarrow	sFID \downarrow	IS \uparrow	Prec. \uparrow	Rec. \uparrow	KDD \downarrow
CFM ($\lambda = 0.05$)	3.61	5.26	211.9	0.817	0.536	0.319
TCFM ($\lambda = 0.10$)	3.82	5.57	211.8	0.813	0.533	0.321

Despite our hypothesis, TCFM underperformed standard CFM across most metrics. The time-weighting did not provide the expected benefit, suggesting that CFM’s contrastive signal remains useful even at low noise levels.

x_0 prediction with velocity loss. We tested the approach from JiT [13], which uses x_0 prediction combined with velocity-based loss formulation. This technique showed promise for pixel-space diffusion models. However, in our latent space setting with INVAE, performance was significantly worse than standard flow matching. This suggests that x_0 prediction objectives may be most beneficial for pixel-space models rather than latent diffusion.

Equilibrium Matching. We attempted to implement Equilibrium Matching [32], which combines energy-based modeling with flow matching. Despite following the methodology, we were unable to reproduce their reported results on our SiT-B/1 architecture with representation alignment. Performance was significantly worse than standard flow matching, suggesting potential incompatibilities between EqM and our architectural choices or training setup.

B.5 Alternative Optimizers

We evaluated alternative optimizers to determine if they could improve upon Adam’s performance. Specifically, we tested Prodigy [17], which provides adaptive learning rate scheduling, and Muon [9], a momentum-based optimizer. Table 8 shows results at 400K iterations.

Table 8: Alternative optimizer ablations at 400K iterations. All experiments use REG + INVAE + SPRINT + RMSNorm + RoPE. Adam with standard hyperparameters performs best.

Optimizer	FID \downarrow	sFID \downarrow	IS \uparrow	Prec. \uparrow	Rec. \uparrow	KDD \downarrow
Adam (baseline)	4.09	6.22	194.2	0.778	0.563	0.368
Prodigy	4.67	5.70	175.1	0.820	0.495	0.367
Muon	48.70	23.34	32.7	0.425	0.506	1.378

Both Prodigy and Muon showed early promise during training with lower initial losses. However, Adam consistently overtook both by 400K iterations. Muon’s performance was particularly poor, plateauing early in training and achieving catastrophically bad final metrics (FID 48.70, KDD

1.378). Prodigy performed better than Muon but still underperformed Adam, particularly on recall (0.495 vs 0.563) and IS (175.1 vs 194.2). These results suggest that for our configuration, standard Adam with well-tuned hyperparameters remains the most reliable choice.

Visual Results

All class-conditional samples below are generated with 250 sampling steps using path-drop guidance with guidance scale 2.5, guidance low threshold 0.10, and guidance high threshold 0.80.

Class 68

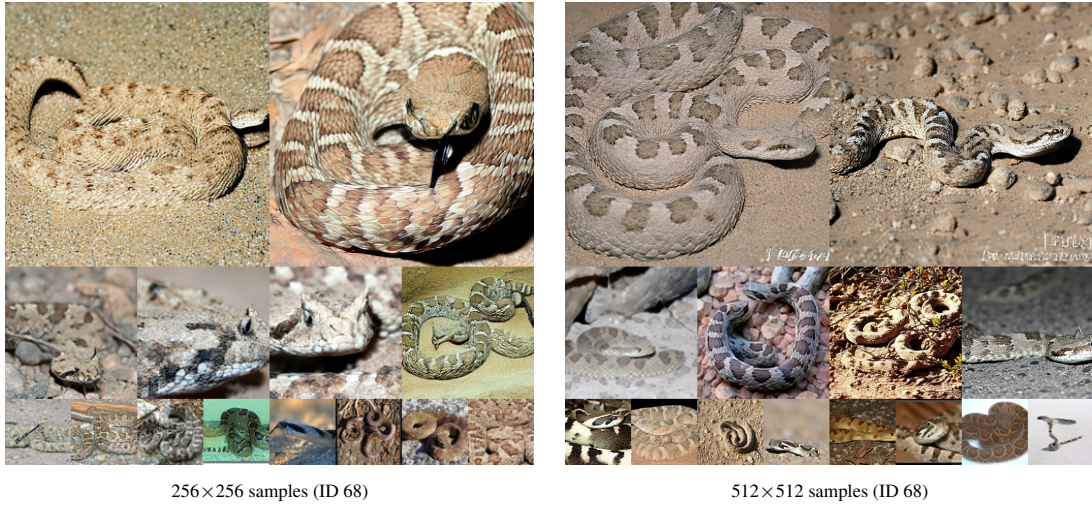


Figure 4: Uncurated SR-DiT-B/1 samples for ImageNet class 68 (sidewinder, horned rattlesnake, *Crotalus cerastes*) at 256×256 and 512×512 resolution.

Class 92

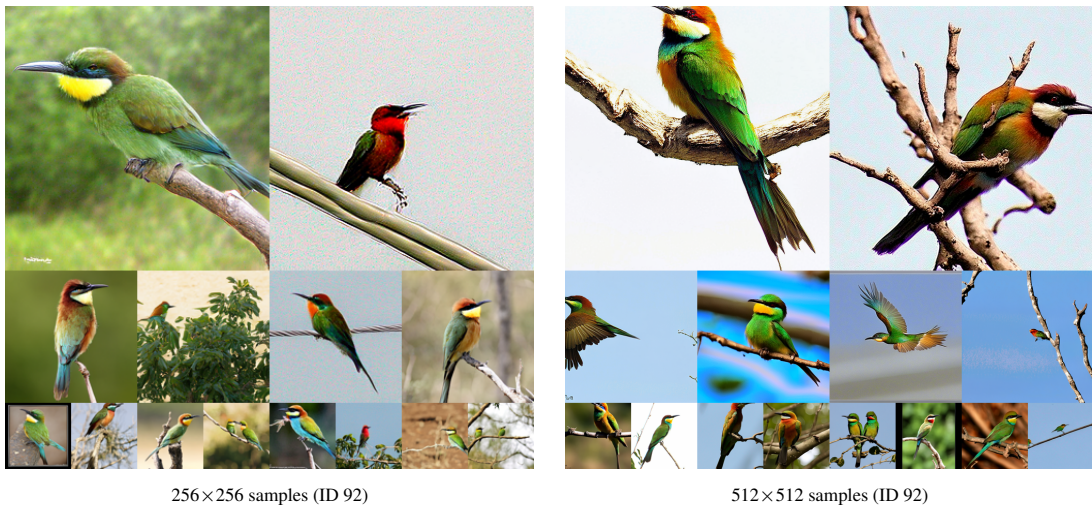


Figure 5: Uncurated SR-DiT-B/1 samples for ImageNet class 92 (bee eater) at 256×256 and 512×512 resolution.

Class 233

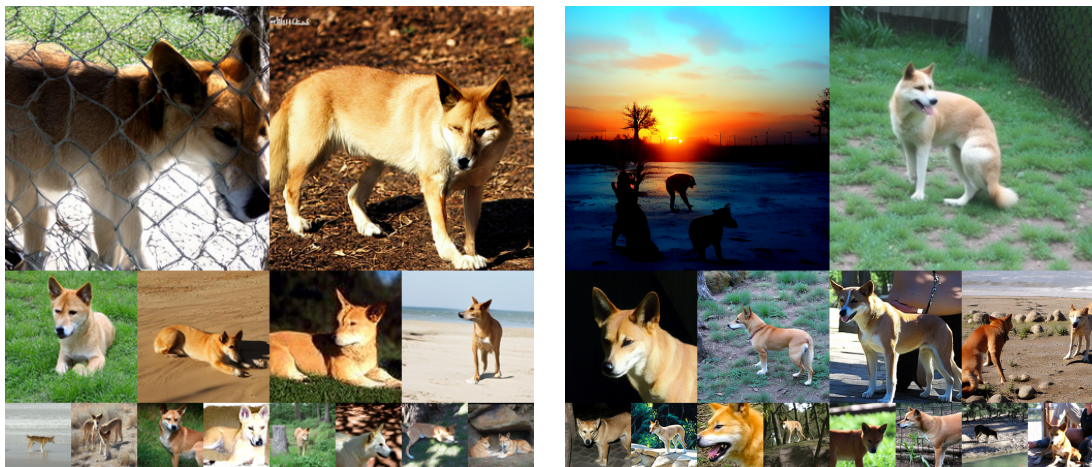


256×256 samples (ID 233)

512×512 samples (ID 233)

Figure 6: Uncurated SR-DiT-B/1 samples for ImageNet class 233 (Bouvier des Flandres, Bouviers des Flandres) at 256×256 and 512×512 resolution.

Class 273



256×256 samples (ID 273)

512×512 samples (ID 273)

Figure 7: Uncurated SR-DiT-B/1 samples for ImageNet class 273 (dingo, warrigal, warragal, Canis dingo) at 256×256 and 512×512 resolution.

Class 283



256×256 samples (ID 283)

512×512 samples (ID 283)

Figure 8: Uncurated SR-DiT-B/1 samples for ImageNet class 283 (Persian cat) at 256×256 and 512×512 resolution.

Class 360



256×256 samples (ID 360)

512×512 samples (ID 360)

Figure 9: Uncurated SR-DiT-B/1 samples for ImageNet class 360 (otter) at 256×256 and 512×512 resolution.

Class 482



256×256 samples (ID 482)

512×512 samples (ID 482)

Figure 10: Uncurated SR-DiT-B/1 samples for ImageNet class 482 (cassette player) at 256×256 and 512×512 resolution.

Class 545



256×256 samples (ID 545)

512×512 samples (ID 545)

Figure 11: Uncurated SR-DiT-B/1 samples for ImageNet class 545 (electric fan, blower) at 256×256 and 512×512 resolution.

Class 721



Figure 12: Uncurated SR-DiT samples for ImageNet class 721 (pillow) at 256×256 and 512×512 resolution.

Class 727



Figure 13: Uncurated SR-DiT samples for ImageNet class 727 (planetarium) at 256×256 and 512×512 resolution.

Class 795

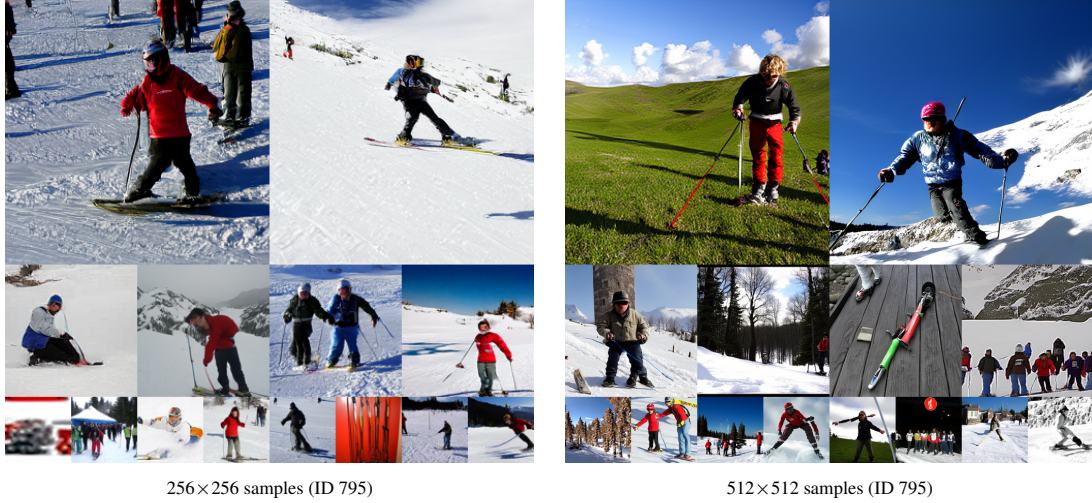


Figure 14: Uncurated SR-DiT samples for ImageNet class 795 (ski) at 256×256 and 512×512 resolution.

Class 839



Figure 15: Uncurated SR-DiT samples for ImageNet class 839 (suspension bridge) at 256×256 and 512×512 resolution.

Class 863



Figure 16: Uncurated SR-DiT samples for ImageNet class 863 (totem pole) at 256×256 and 512×512 resolution.

Class 929

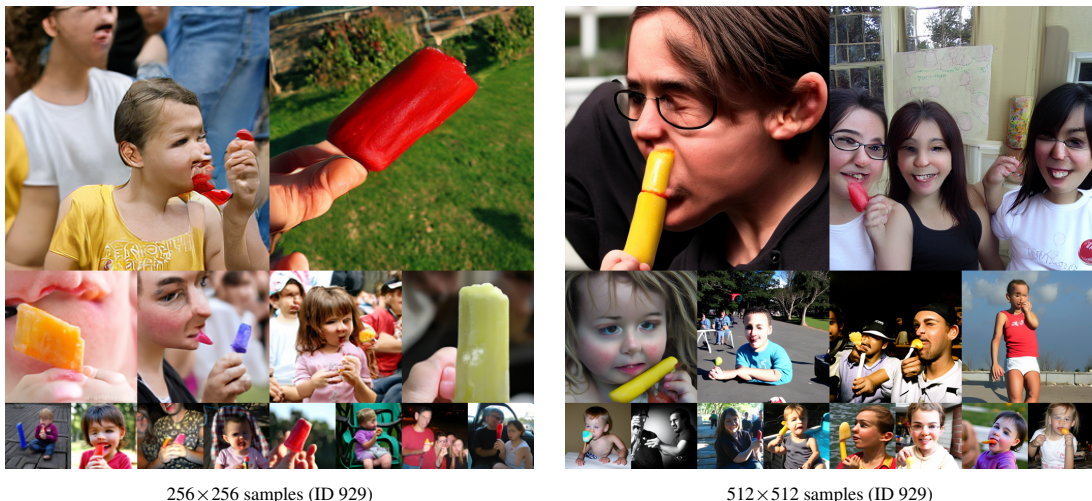


Figure 17: Uncurated SR-DiT samples for ImageNet class 929 (ice lolly, lolly, lollipop, popsicle) at 256×256 and 512×512 resolution.

Class 944



256×256 samples (ID 944)

512×512 samples (ID 944)

Figure 18: Uncurated SR-DiT samples for ImageNet class 944 (artichoke, globe artichoke) at 256×256 and 512×512 resolution.

Class 974



256×256 samples (ID 974)

512×512 samples (ID 974)

Figure 19: Uncurated SR-DiT samples for ImageNet class 974 (geyser) at 256×256 and 512×512 resolution.

Class 984



256×256 samples (ID 984)

512×512 samples (ID 984)

Figure 20: Uncurated SR-DiT samples for ImageNet class 984 (rapeseed) at 256×256 and 512×512 resolution.

Class 991



256×256 samples (ID 991)

512×512 samples (ID 991)

Figure 21: Uncurated SR-DiT samples for ImageNet class 991 (coral fungus) at 256×256 and 512×512 resolution.